International Journal of Medical Imaging
2025, Vol. 13, No. 1, pp. 7-19
https://doi.org/10.11648/j.ijmi.20251301.12

Research Article

Sparse-view CT Image Reconstruction Using the Logarithmic Barrier Based Interior Point Method

Heping Xu*

Department of Radiation Oncology, Indiana University, Indianapolis, USA

Abstract

This work aims to develop a logarithmic barrier based interior point method capable of reconstructing CT images using under-sampled sinogram data. Unlike other compressed sensing methods, the proposed method obviates the need of the regularization parameter in the objective function. Feasibility of the algorithm and quality of the reconstructed images were examined. Methods: The sinogram data were simulated through Radon-transforming clinical CT images. The noise was added based on the Poisson and Gaussian models. The basic elements of the proposed method, logarithmic barrier (LB) method, were introduced. The relative Root-Mean-Squared Error (rRMSE) was used to evaluate the image reconstruction accuracy. The noise of the images was assessed using the Peak Signal-to-Noise Ratio (PSNR) and Mean Squared Error (MSE). Results: The PSNR, rRMSE, MSE were compared among fvFBP (full-view Filtered-Backprojection), svFBP (sparse-view Filtered-Backprojection), BB (Barzilai-Borwein), and LB methods for brain, head and neck, lung, prostate, and leg sites. The reconstructed images from svFBP suffered severe streak artifacts. The LB method was capable of reconstructing images of quality comparable to quality of those images obtained from other compressed sensing-based methods such as the BB method. Conclusion: It has been demonstrated that the compressed sensing technique based on the logatirhmic barrier method is capable of recovering satisfactory images from under-sampled projection data. This method obviates the need of the regularization parameter that specifies the relative weight between the data fidelity and total variation terms in the objective function. Insights have been gained as to implementing the proposed method for clinical imaging applications.

Keywords

Compressed Sensing, CT Reconstruction, Interior Point Method, Medical Imaging

1. Introduction

Computed Tomography (CT) has witnessed wide applications in modern medicine, ranging from diagnostic radiology to therapeutic radiation oncology [1]. Every year, a total of approximately 300 million CT scans are conducted globally and the number of CT examinations increase by 4% annually and globally [2]. In addition, millions of cancer patients who have been treated using modern IGRT (Image Guided Radiotherapy) undergo CBCT (Cone Beam CT) in order to achieve high accuracy in treatment positions [3]. While modern CT imaging dose per scan and associated health risk is low, patients and medical staff gain additional benefit when CT imaging dose is further reduced while maintaining the image quality that provides required clinical information [4]. The most widely used commercial

*Corresponding author: hx14@iu.edu (Heping Xu)

Received: 19 January 2025; **Accepted:** 5 February 2025; **Published:** 20 February 2025

reconstruction algorithm is the filtered backprojection method (FBP), which can be applied to both 2D and 3D image reconstruction [5, 6]. Other recently commercially available algorithms are statistically based formulations using iterative methods to reconstruct images [7-9]. While the FBP is simple and fast, an issue associated with the FBP is that the number of projections needed is larger than that is minimally required in order to obtain accpetable noise suppresion and spatial resolution. A larger number of projections translates to additional imaging dose to healthy organs/tissue in patients, which may be a clinical concern especially in the era of increased use of CT in diagnostic radiology and cone beam CT (CBCT) in the image guided radiotherapy in radiation oncology.

Much research effort has been channeled into methods dedicated to decreasing imaging dose in CT scans. Dose management and reduction are achieved through optimizing CT imaging parameters in clinical protocols guided by the ALARA (As Low As Reasonably Achievable) principle. This includes optimized mAs/kV combination, employment of Automatic Exposure Control [10]. An alternative apporach is to use reduced mAs or reduced number of projection data to perform image reconstruction [10]. While FBP is widely used to perform reconstruction with sufficient data (in terms of the number of detected photons and the number of projection data), it is incapable of achieving satisfactory image quality with reduced mAs and reduced number of projection data due to excessive noise and severe streak artifacts. Model based iterative method [11, 12] and penalized weighted least squares method [13-15] were explored to mitigate high noise level and to reduce streak artifacts [16].

Recently, there has been a growing interest in applying the compressed sensing technique to CT reconstruction from under-sampled projection data. The compressed sensing technique draws on the theory that the image can be reconstructed at a sampling rate less than the Nyquist criteria provided the original image is sparse in some transformed domain [17-20]. Extensive research exists that addresses CT reconstruction, 4D CBCT [21], temporal cardiac CT [22], perfusion CT [23, 24], based on the compressed sensing technique. It has been demonstrated that this technique has clinical potential to reduce imaging dose [25]. The image quality can be further improved in some situations if prior images are available and included in the optimization objectives [26, 27].

In the compressed sensing technique, image reconstruction is formulated as a mathematical optimization problem [17, 18, 28, 29]. The reconstructed image is the sparsest possible solution under some transformed domain, subject to the constraints that the image is consistent with the measurements. The sparsifying operation is typically the gradient computation on the image. The objective function, which is the L_1 norm of the gradient of the image, is equal to the total variation of the image. Choice of L_1 norm instead of L_0 norm renders the mathematical optimization computationally tractable. The optimization problem is formulated as follows: $\min_x TV(x)$ subject to $Ax = b$ and $x \geq 0$. The reconstructed image is the one that minimizes the total variation and is not inconsistent with the measurements.

Under this basic formalism, a number of CT reconstruction algorithms have been proposed to further improve on the reconstructed image quality. Total variation was replaced with a non-local one that allows for non-uniform weight penalization in reconstruction [30]. The adaptively re-weighted total variation was proposed to further reduce the required number of projections as it is a closer approximation to the L_0 norm [31]. Various algorithms to find the minimum of the cost function were developed. A few examples are provided here: accelerated fast iterative shrinkage threshold-ing algorithms [32]; first order method [33]; second order method using Hessian penalty [34]; Barzilai-Borwein method [35]; accelerated barrier optimiation compressed sensing method [36, 37]. More advanced teniques invoke the use of curvelet, wavelet, and dictionary learning methods [38-40]. Tight frame was used to take advantage of parallel computing of GPUs [41]. Colony based optimization was also successfully implemented [42]. Data-driven regularization methods combined with deep neural networks have recently been explored and shown potential to succeed [43-45].

Many existing optimization solvers convert the constrained problem to an unconstrained problem by combining the objective function and the data fidelity term through a regularization parameter that determines the relative importance between them [30, 32, 35, 36, 46, 47]. Those methods demonstrate that satisfactory reconstruction can be achieved with a carefully chosen regularization parameter that balances the relative importance of the total variation and the data fidelity term. However, the regularization parameter (weighting factor) is one of the most influential parameters affecting the image quality [35, 36]. Some researchers have conducted investigation on optimizing values of the weighting factor [35, 48, 49]. It is likely that the factor depends on the number of projections, individual patients, and specific sites. This presents significant practical limitations to its application in clinics as those values are not known a priori. This challenge leads us to explore a new direction of methods that obviate the use of the regularization parameter. We propose that the interior point method can be used to achieve this. Instead of using the gradient descent method to minimize the functions, the Newton's method will be used to find the minimum for the sub-problem optimizations in the interior point method. Our previous preliminary results indicate that this is a feasible approach [50]. This method is computationally intensive.

In this article, a brief description of the proposed logarithmic barrier method is given. The posposed method is evaluated using the digital Shepp-Logan phantom, and CT images acquired from the anatomical sites of lung, brain, head and neck, prostate, and leg, followed by disccusion and conclusion.

2. Materials and Methods

2.1. Generation of Sinograms by Simulation

The 2D Shepp-Logan digital phantom (MATLAB®) composed of several ellipses radiologically resembling bones, soft tissues and air was used for the phantom study. Five clinically relevant images were chosen to represent common treatment sites: brain, head and neck (HN), lung, prostate and leg. They were acquired from the GE light-speed 16 CT scanner following the in-house protocols. As the purpose of this study is to explore the fan-beam based CT image reconstruction algorithms, one CT slice for each site was selected to generate sinograms. All images were properly anonymized in accordance with the data management guidelines within the author's institution. The image resolution was 512×512 pixels. The projection data were simulated using mono-energetic fan beam geometry on the CT scanner with a circular orbit. The source-to-axis distance was 100.0 cm and the source-to-detector distance was 150.0 cm. The projection data were generated by the Radon-transform of the 2D CT images. The X-ray detection system was modeled as an array of 370 detectors. The reconstructed 2D image resolution was of 512×512 pixel resolution. Subsets of 47, 67, 97, 137 number of the equally and angularly spaced projections were selected for reconstruction.

2.2. Noise Model

The sinograms were generated under noise-free condition. To characterize the algorithm's performance under the noisy sonograms, a well-known X-ray noise model for CT was used [24, 51]. For the i^{th} detector bin, the line integral is $y_i = -\ln\frac{I_i}{I_{i0}}$, where I_{i0} and I_i are the number of incident photons and the number of detected photons at the i^{th} detector bin, respectively. The noisy measurement b_i at the i^{th} bin was obtained through $\Delta y_i = Poisson(I_{i0}\exp(-y_i)) + Normal(0, \sigma_e^2)$, where the first term accounts for the noise from photon counting characterized by the Poisson statistics, and the second term allows for background electronic noise variance characterized by the Gaussian distribution with variance σ_e^2. The Gaussian noise can be incorporated in the Poisson term as follows: $\Delta y_i = \lambda \cdot Poisson(I_{i0}\exp(-y_i))$ through a factor $\lambda > 1$. In this study a uniform number of incident photons was used for all detectors. The number of incident photons typically ranges from 10^4 to 10^6.

2.3. Logarithmic Barrier Formulation [52]

Consider the equality constrained TV minimization problem:

$$\min_x TV(x) \text{ subject to } Ax = b \text{ and } x \geq 0 \tag{1}$$

where x is the image vector obtained by flattening the image of dimension $n \times n$ via the column-major order, A is the system operator (i.e., the Radon transform for CT image reconstruction), b is the measured sinogram data.

Define the operator D_i such that $D_i x = (D_{h,i}x \quad D_{v,i}x)^T$, $D_{h,i}x = x_{i+1} - x_i$ and $D_{v,i}x = x_{i+n} - x_i$ where $i = 1, 2, 3, \ldots, n$.

D_v can be reformatted as a diagonal matrix: $D_v = diag(d_v \quad \ldots \quad d_v)$ consisting of n copies of d_v

where $d_v = \begin{pmatrix} -1 & 1 & & & & \\ & -1 & 1 & & & \\ & & \ddots & \ddots & & \\ & & & -1 & 1 & \\ & & & & -1 & 1 \\ & & & & & 0 \end{pmatrix}$ is of size $n \times n$.

D_h can be represented as follows:

$D_h = \begin{pmatrix} -I_n & I_n & & & & \\ & -I_n & I_n & & & \\ & & \ddots & \ddots & & \\ & & & -I_n & I_n & \\ & & & & -I_n & I_n \\ & & & & & 0 \end{pmatrix}$ where I_n is an identity matrix of size $n \times n$.

The gradient at pixel x_i is the Euclidean norm of $D_i x$. The isotropic total variation is $TV(x) = \sum_{i=1}^{N} \| D_i x\|_2$

Using slack variables t_i, Problem (1) can be transformed to a second-order cone problem:

$$\min_{x,t} \sum_{i=1}^{N} t_i \text{ s.t. } ||D_i x||_2 - t_i \leq 0 \text{ and } Ax = b \text{ and } x \geq 0 \tag{2}$$

where N is the total number of image pixels.

The inequality constraints $||D_i x||_2 - t_i \leq 0$ can be incorporated in the objective function as follows. Define $f_i = \frac{1}{2}(\left||D_i x|\right|_2^2 - t_i^2)$, where $i = 1, 2, \ldots, N$. Using $-f_i$ as the argument of the log function $-\ln(f_i)$, problem (2) can be transformed into a series of linearly constrained sub-problems indexed by the log-barrier iteration integer k:

$$\min_{x,t} f = \sum_{i=1}^{N} t_i + \frac{1}{\tau_k}\sum_{i=1}^{N}(-\ln(-f_i)) \text{ s.t. } Ax = b \text{ and } x \geq 0 \tag{3}$$

where τ_k is the log-barrier parameter indexed by k.

It is shown [52] that the inequality constraints are in the

domain of the log functions and are incorporated into the objective function weighted by τ_k which are a set of monotonically increasing parameters as the function of k. This is known as the log-barrier method. Larger τ_k indicates that Problem (1) is more accurately represented by this approximation. During optimization, x is chosen such that it is not outside the feasible region. This condition ensures that the argument in the log function is always positive. The sub-problems are solved via the Newton's method.

Pseudocode for $\min_{x,t} f = \sum_{i=1}^{N} t_i + \frac{1}{\tau_k}\sum_{i=1}^{N}(-\ln(-f_i))$ s.t. $Ax = b$ and $x \geq 0$:

Since the pseudocode is illustrated for a sub-problem, the sub-problem indexing k is omitted.

Parameter setup:

$LB_{tol} = 1.0 \times 10^{-7}$ is the duality gap that determines tolerance for log-barrier method;

$\mu = 10$ determines decrease rate for τ;

N = total number of pixels in an image;

Initialization: x, t are obtained from FBP reconstruction, τ=initial total variation;

$LB_{iter} = \lceil((\ln(N) - \ln(LB_{tol}) - \ln(\tau))/\ln(\mu)\rceil$

Pseudocode:

for $i = 1$ to LB_{iter}

$N_{iter} = 0$

$done = FALSE$

$Newton_{tol} = LB_{tol}$ (Set tolerance of Newton's method)

$Newton_{MaxIter} = 80$ (Set maximum number of iterations for Newton's method)

while NOT $done$

Evaluate Hessian and gradient of the sub-problem

Using the generalized minimal residual (GMRES) method to solve the linear equation to find dx and dt

Determine the minimum step-sizes for x and t such that they lie in the interior region

Backtracking line search to find next x and t in the feasible region

$N_{iter} = N_{iter} + 1$

$done = (lambda < Newton_{tol})\ OR\ (N_{iter} > Newton_{MaxIter})$

end

$\tau = \tau\mu$ (Increasing τ by a factor of μ)

end

2.4. Methods to Compare with the Log-barrier Method

2.4.1. Barzilai-Borwein Formulation [35, 36, 53]

The reconstruction problem is formulated as the minimization of the following objective function subject to the positivity constraint of each pixel:

$$f(x) = TV(x) + \frac{\lambda}{2}||Ax - b||_2^2 \quad (4)$$

Similar to the conventional steepest descent method, the descent direction p was determined by the gradient of the objective function. An adaptive choice of the step size was made between α^1 and α^2 determined by an adaptation constant κ between 0 and 1. α^1 and α^2 are calculated as: $\alpha_n^1 = \frac{(f_n - f_{n-1})^T(f_n - f_{n-1})}{(f_n - f_{n-1})^T(p_n - p_{n-1})}$ and $\alpha_n^2 = \frac{(f_n - f_{n-1})^T(p_n - p_{n-1})}{(p_n - p_{n-1})^T(p_n - p_{n-1})}$ respectively. The step size is chosen as: $\alpha_n = \begin{cases} \alpha_n^2 \ if\ \alpha_n^1\alpha_n^2 < \kappa \\ \alpha_n^1 \ otherwise \end{cases}$

This choice of step size improves the convergence speed of the conventional BB (Barzilai-Borwein) method in which either α^1 or α^2 is used throughout the optimization. The optimization terminates when either the maximum number of iterations is reached or the change in successive reconstructed image vectors is less than the pre-set tolerance.

2.4.2. Full-view Filtered-BackProjection (fvFBP) and Sparse-view Filtered-BackProjection (svFBP)

The full-view Filtered-BackProjection method employs standard FBP to reconstruct the image using 937 number of projections. The sparse-view Filtered-BackProjection method uses 47, 67, 97, and 137 numbers of projections. Comparison of various reconstruction methods is made against results obtained from fvFBP instead of ground truth images.

2.5. Evaluation Metrics

2.5.1. Reconstruction Accuracy

The relative Root-Mean-Square Error ($rRMSE$) is defined as the mean squared percent error of the reconstructed pixel values against the ground truth pixel values:

$$rRMSE = \sqrt{\frac{\sum_{j=1}^{J}(x_j - x_{j,gt})^2}{\sum_{j=1}^{J}(x_{j,gt})^2}},$$

where x_j represents the j^{th} pixel value, the subscript gt represents the associated pixel values are from the ground truth image, J represents the total number of pixels in the image.

2.5.2. Noise Metrics

Two metrics were used to evaluate the image quality related to the presence of noise. The Peak Signalto-Noise Ratio ($PSNR$) is defined as:

$$PSNR = 10\log_{10}\left(\frac{MAX^2(x_{gt})}{(\sum_{j=1}^{J}(x_j - x_{j,gt})^2)/(J-1)}\right)$$

where $MAX(x_{gt})$ represents the maximum pixel values in the ground truth image. The Mean Squared Error (MSE) is defined as:

$$MSE = \frac{1}{\bar{x}_{gt}}\sqrt{(\sum_{j=1}^{J}(x_j - x_{j,gt})^2)/(J-1)}$$

where $\bar{x}_{gt}$ represents the average pixel value of the ground truth image, J represents the total number of pixels in the image.

3. Results

Figure 1 and Figure 2 show the reconstructed 2D images from the 67 noiseless projections. The Shepp-Logan phantom and five anatomical sites were employed: brain, head and neck, lung, prostate, and leg. Figure 3 and Figure 4. show the reconstructed 2D images from the 67 noisy projections for more realistic clinical applications. Figures 5 and 6 (Figures 7 and 8) show the reconstructed 2D images from 137 (47) noisy projections for the Shepp-Logan phantom and five anatomical sites. In this article, the noise is simulated using 1×10^5 photons.

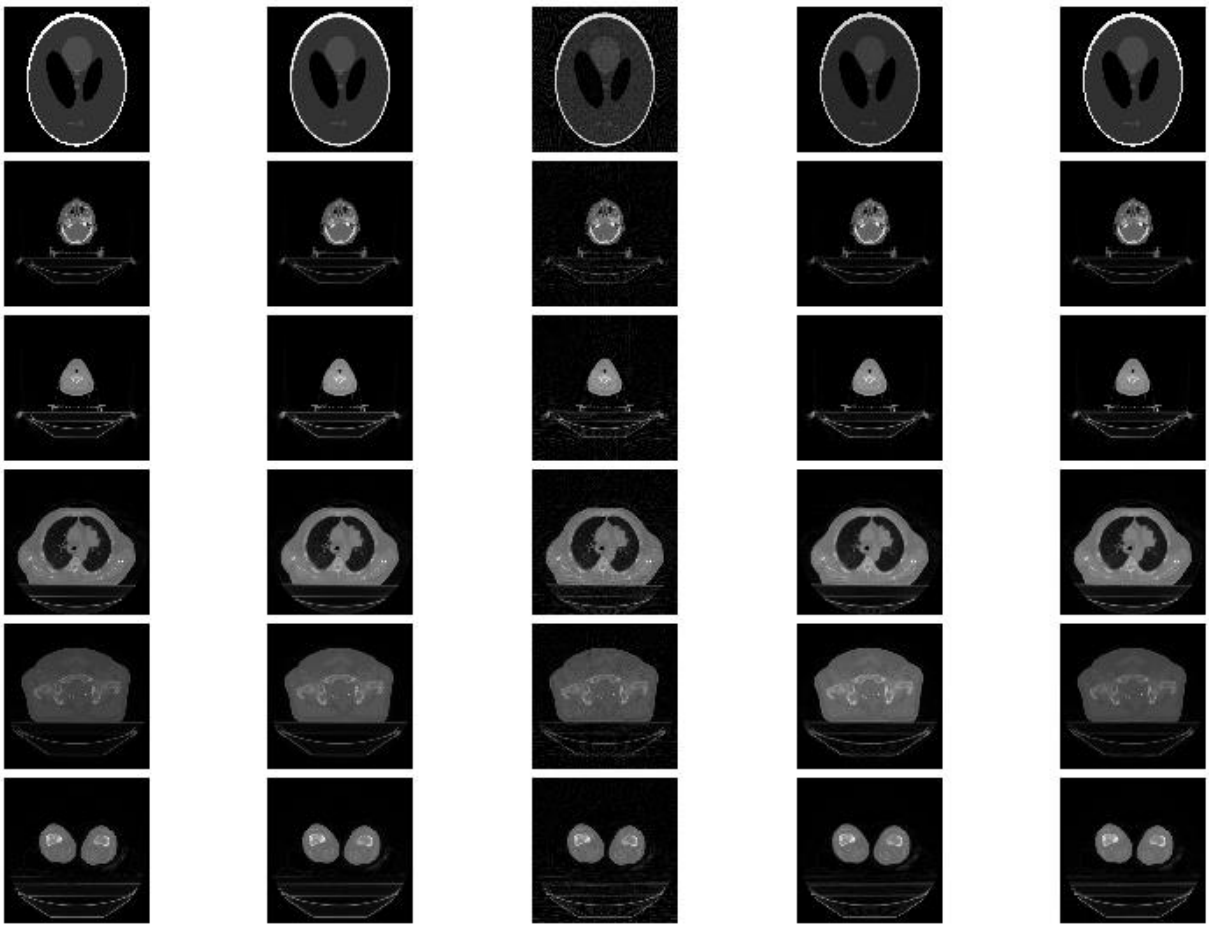

Figure 1. *The image reconstruction results from noiseless projection data for Shepp-Logan phantom (1st row), brain image (2nd row), head-and-neck image (3rd row), lung image (4th row), prostate image (5th row), and leg image (6th row). The first column shows the ground truth images. The second column shows the result from the full-view FBP (937 projections). The third column shows the result from the sparse-view FBP (67 projections). The fourth column shows the result from the Barzilai-Borwein method (67 projections). The fifth row shows the result from the log-barrier based interior point method (67 projections).*

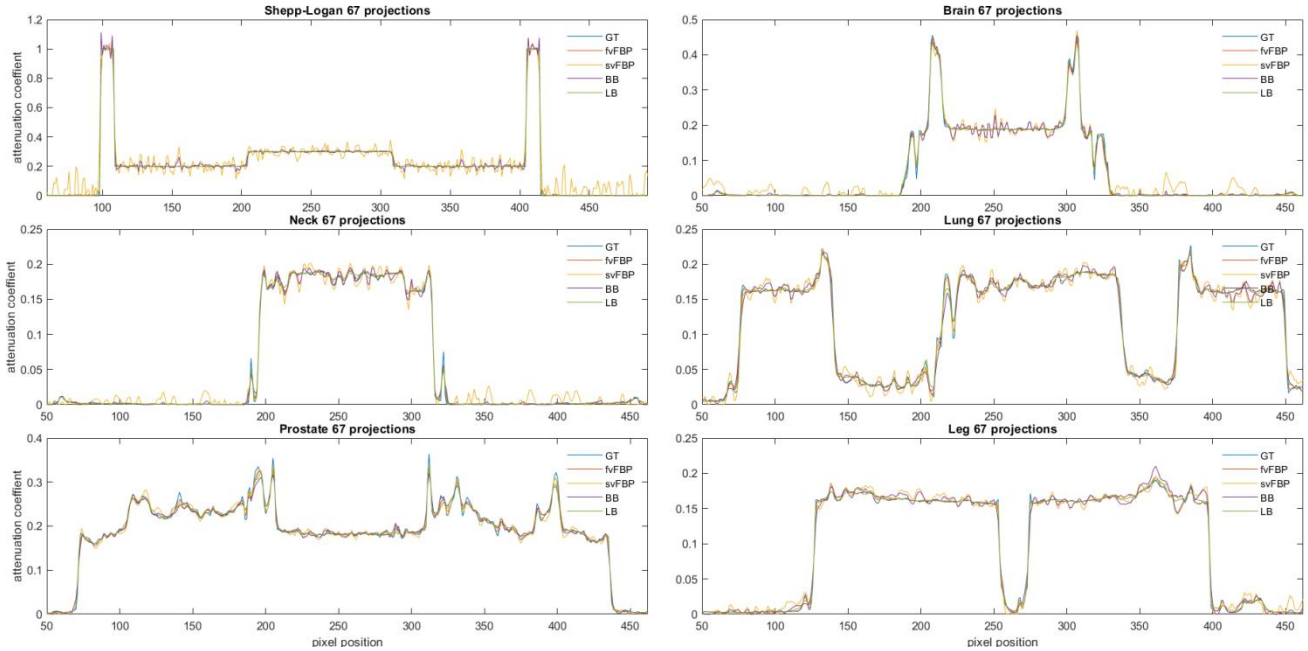

Figure 2. *Horizontal profiles through the center of the images (same images in Figure 1). The ground truth and the results from four methods are represented by different colors. (Images are reconstructed from noiseless data of 67 projections except those reconstructed from fvFBP which uses 937 projections).*

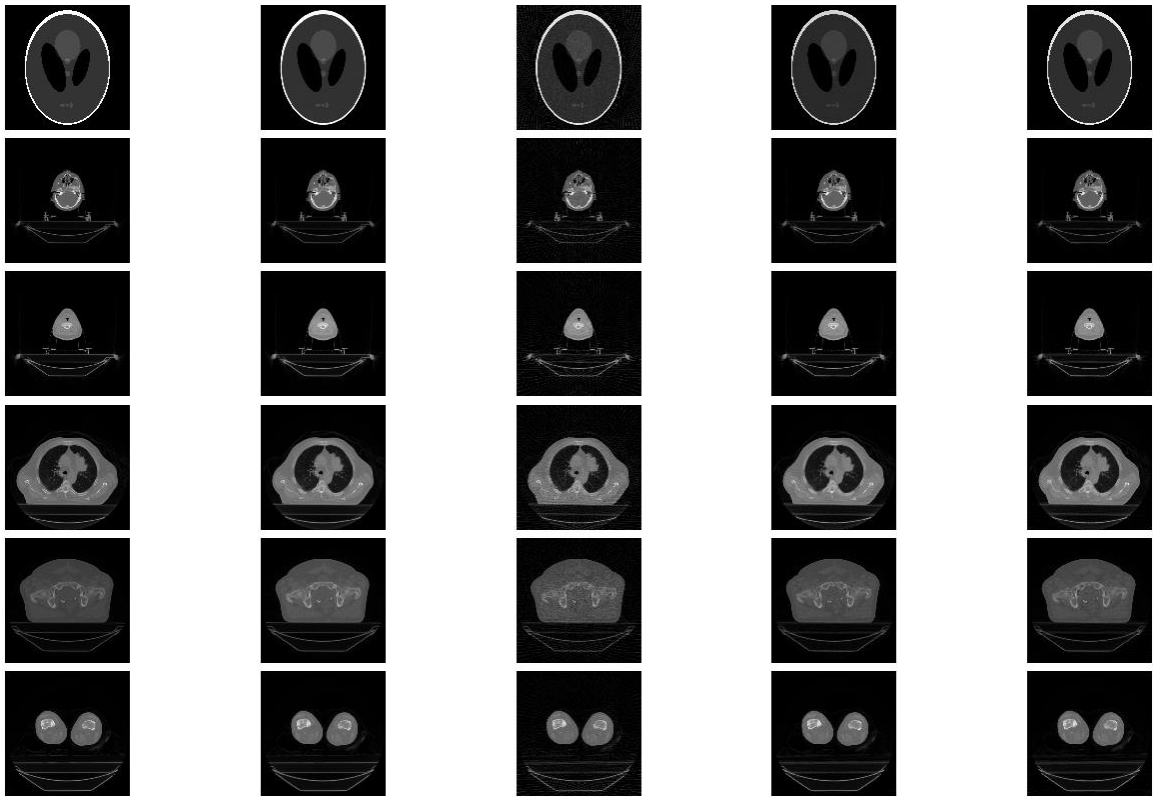

Figure 3. *The image reconstruction results from noisy projection data for Shepp-Logan phantom (1st row), brain image (2nd row), head-and-neck image (3rd row), prostate image (4th row), prostate image (5th row), and leg image (6th row). The first column shows the ground truth images. The second column shows the result from the full-view FBP (937 projections). The third column shows the result from the sparse-view FBP (67 projections). The fourth column shows the result from the Barzilai-Borwein method (67 projections). The fifth row shows the result from the log-barrier based interior point method (67 projections).*

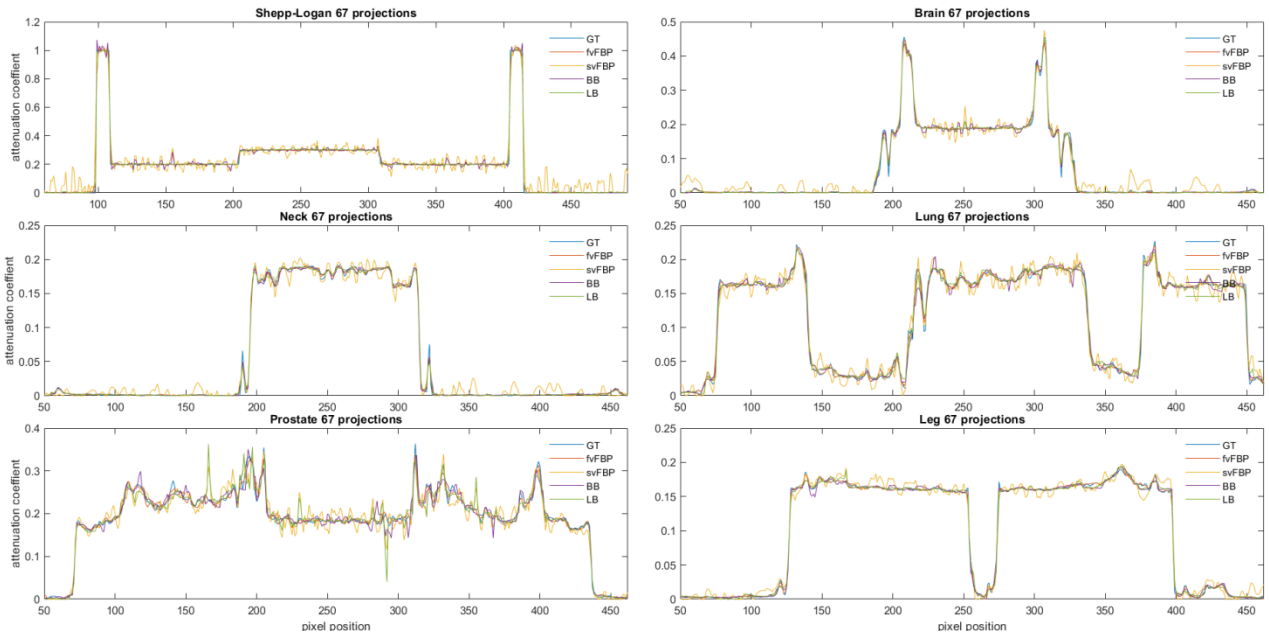

Figure 4. *Horizontal profiles through the center of the images (same images in Figure 3). The ground truth and the results from four methods are represented by different colors. (Images are reconstructed from noisy data of 67 projections except those reconstructed from fvFBP which uses 937 projections).*

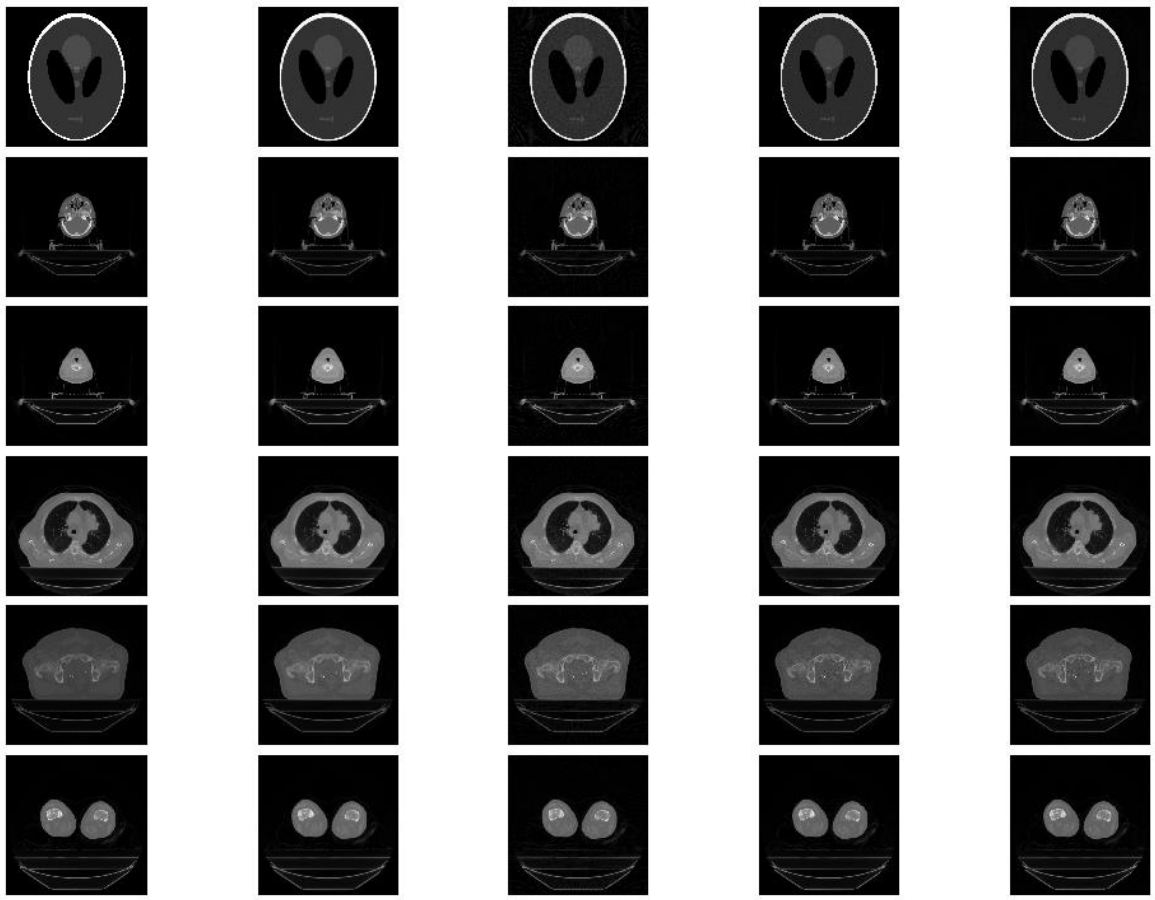

Figure 5. *The image reconstruction results from noisy projection data for Shepp-Logan phantom (1st row), brain image (2nd row), head-and-neck image (3rd row), prostate image (4th row), prostate image (5th row), and leg image (6th row). The first column shows the ground truth images. The second column shows the result from the full-view FBP (937 projections). The third column shows the result from the sparse-view FBP (137 projections). The fourth column shows the result from the Barzilai-Borwein method (137 projections). The fifth row shows the result from the log-barrier based interior point method (137 projections).*

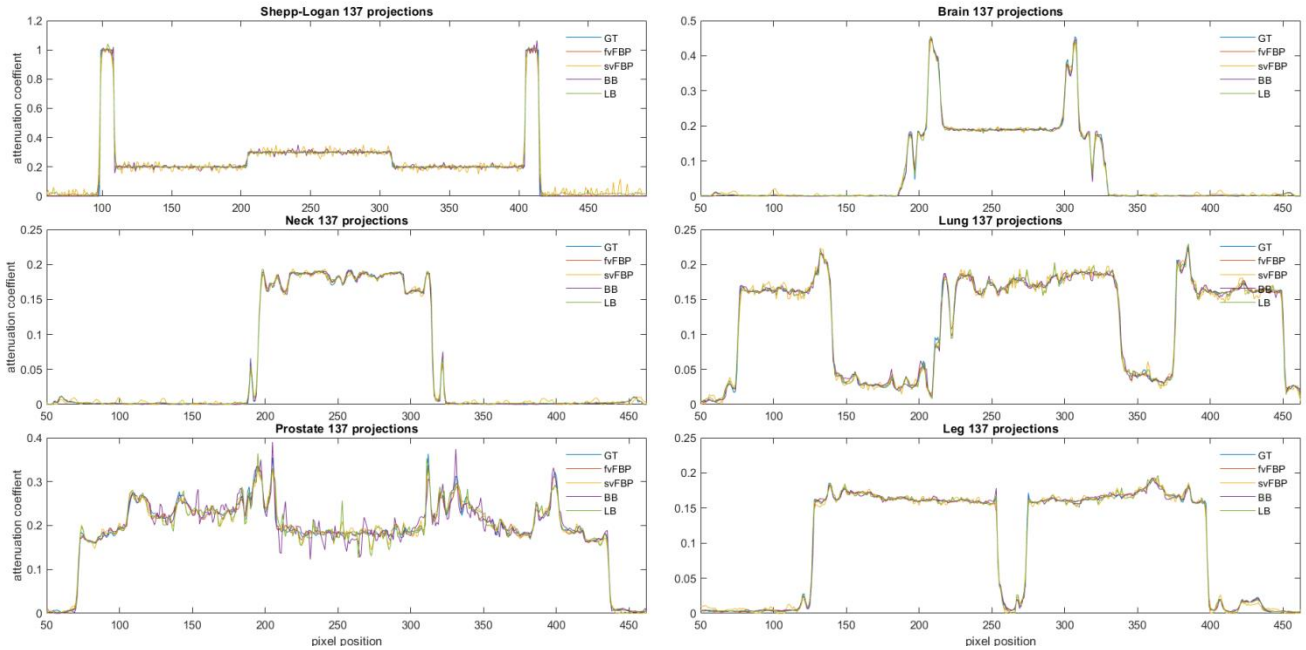

Figure 6. *Horizontal profiles through the center of the images (same images in Figure 5). The ground truth and the results from four methods are represented by different colors. (Images are reconstructed from noisy data of 137 projections except those reconstructed from fvFBP which uses 937 projections).*

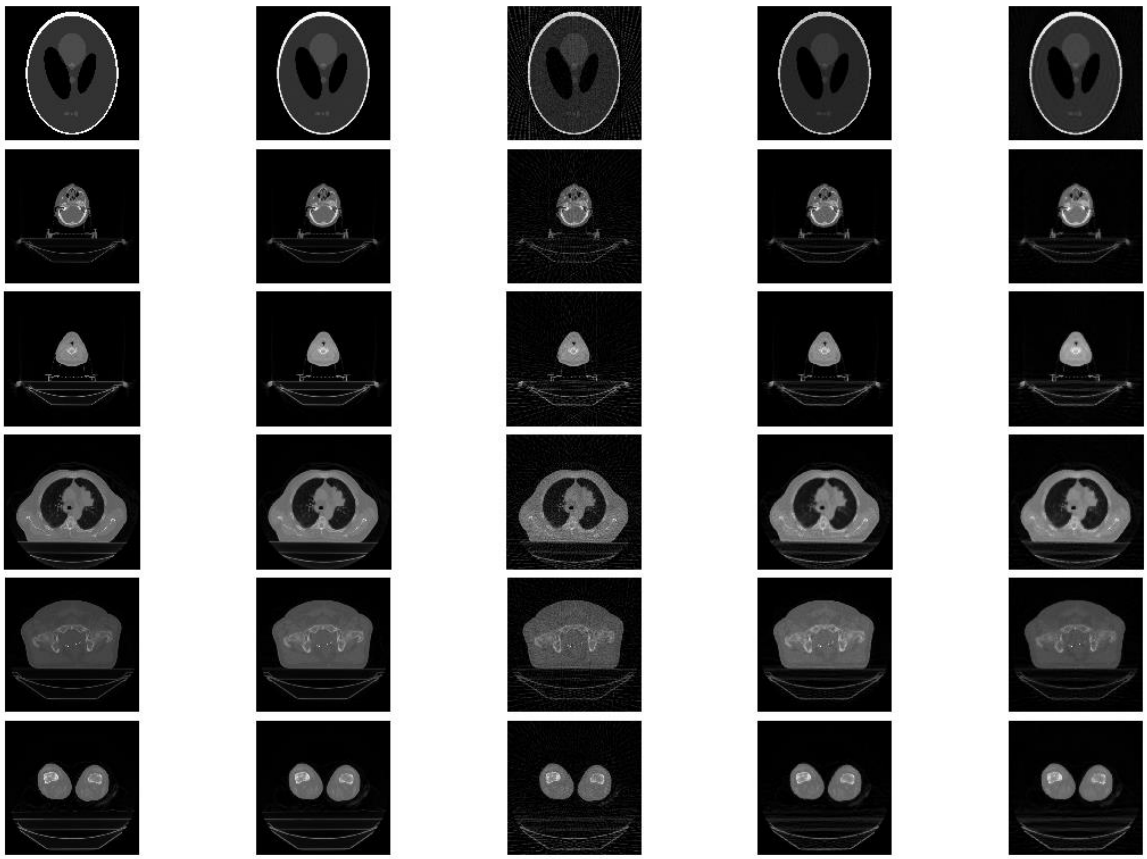

Figure 7. *The image reconstruction results from noisy projection data for Shepp-Logan phantom (1st row), brain image (2nd row), head-and-neck image (3rd row), prostate image (4th row), prostate image (5th row), and leg image (6th row). The first column shows the ground truth images. The second column shows the result from the full-view FBP (937 views). The third column shows the result from the sparse-view FBP (47 projections). The fourth column shows the result from the Barzilai-Borwein method (47 projections). The fifth row shows the result from the log-barrier based interior point method (47 projections).*

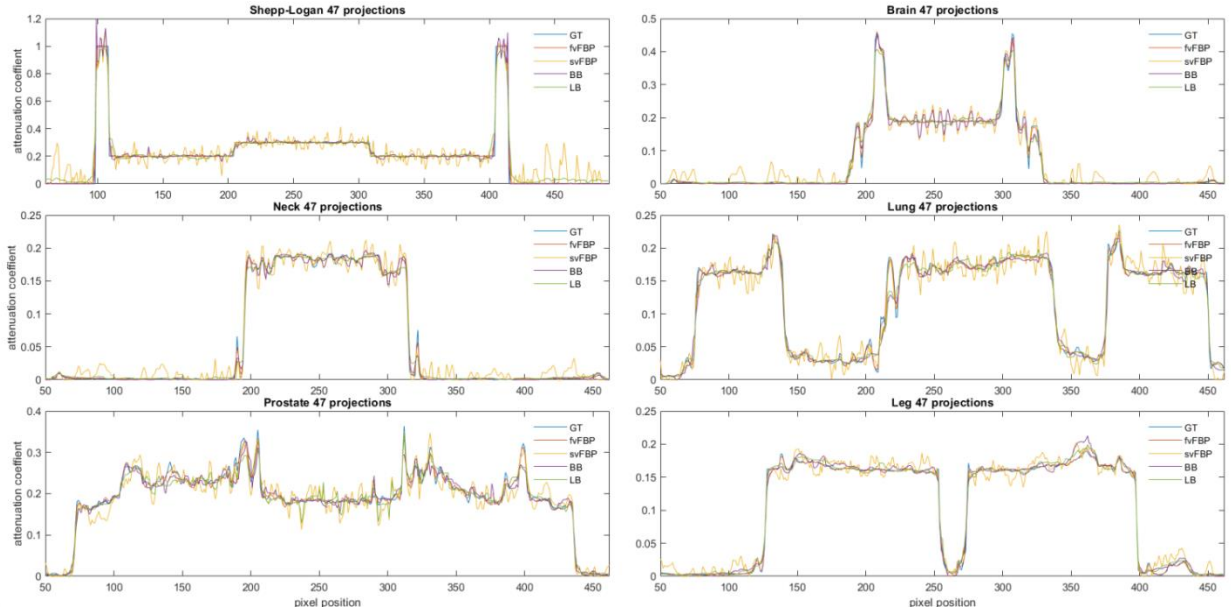

Figure 8. *Horizontal profiles through the middle of the images (same images in Figure 7). The ground truth and the results from four methods are represented by different colors. (Images are reconstructed from noisy data of 47 projections except those reconstructed from fvFBP which uses 937 projections).*

Table 1. *The reconstruction accuracy metric (rRMSE) and image quality metrics (PSNR and MSE) for images reconstructed from algorithms: fvFBP, svFBP, BB, and LB for the Shepp-Logan phantom and five anatomical sites. The number of the noisy data projections used for image reconstruction is 67.*

Metrics	Sites	Algorithms			
		fvFBP	svFBP	BB	LB
PSNR		42.73	24.69	39.12	40.24
MSE $(\times 10^{-3})$	Shepp-Logan	0.5056	0.9229	0.2841	0.1540
rRMSE		0.1293	0.2360	0.0726	0.0394
PSNR		41.699	29.57	38.377	37.553
MSE $(\times 10^{-3})$	Brain	0.4076	1.7387	0.6429	0.7372
rRMSE		0.0688	0.2778	0.1008	0.1109
PSNR		41.5294	29.5787	38.0411	36.3425
MSE $(\times 10^{-3})$	Neck	0.3846	1.6631	0.6295	0.8429
rRMSE		0.0681	0.2698	0.1018	0.1238
PSNR		42.1023	29.6927	36.2358	36.1369
MSE $(\times 10^{-3})$	Lung	0.1165	0.4862	0.2289	0.2315
rRMSE		0.0353	0.1473	0.0693	0.0701
PSNR		44.2461	31.2153	37.8093	37.012
MSE $(\times 10^{-3})$	Prostate	0.1199	0.5376	0.2516	0.2758
rRMSE		0.0377	0.1690	0.0791	0.0867
PSNR		42.8442	30.4144	37.7135	35.551
MSE $(\times 10^{-3})$	Leg	0.2157	0.9022	0.3894	0.4995
rRMSE		0.0480	0.2009	0.0867	0.1112

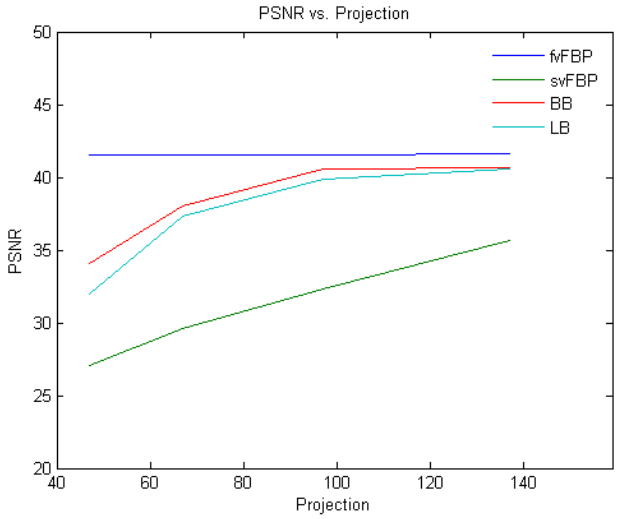

Figure 9. *Comparison of PSNR of the images reconstructed from svFBP, BB, and LB against that of the images reconstructed from fvFBP as a function of the number of noisy data projections for head and neck site.*

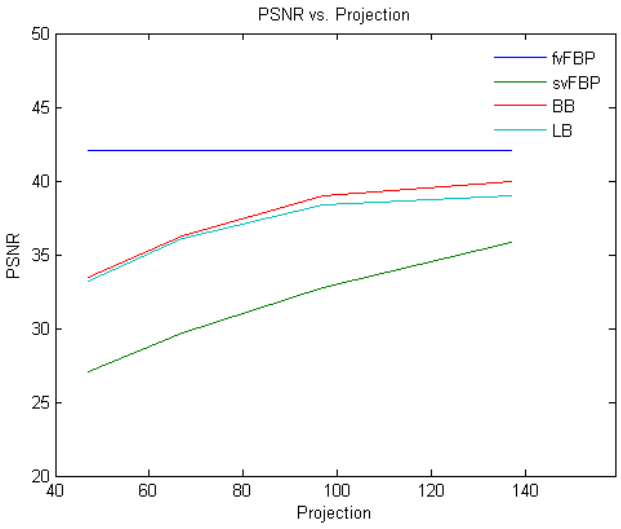

Figure 10. *Comparison of PSNR of the images reconstructed from svFBP, BB, and LB against that of the images reconstructed from fvFBP as a function of the number of noisy data projections for lung site.*

As can be seen, the proposed algorithm performs well and displays robustness with respect to the typical noise level encountered in clinical applications. Reconstructed images from 47 projections display significant streak artifacts using svFBP. The BB and LB methods were not able to reduce this type of artifacts to a visually unnoticeable level, which is also supported by the PSNR values indicated in Figure 9 (for head and neck site) and Figure 10 (for lung site). The PSNR values are illustrated against the Shepp-Logan phantom and five sites for algorithms of fvFBP, svFBP, BB, and LB in Figure 11.

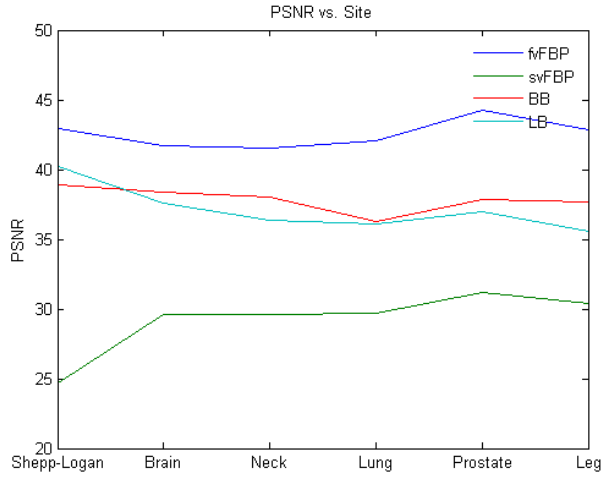

Figure 11. *Comparison of PSNR of the images reconstructed from svFBP, BB, and LB against that of the images reconstructed from fvFBP as a function of various sites. The number of the noisy data projections used for image reconstruction is 67.*

Table 1 shows the reconstruction accuracy metric (rRMSE) and image quality metrics (PSNR and MSE) calculated for images reconstructed from algorithms: fvFBP, svFBP, BB, and LB methods using 67 noisy projections. The svFBP is incapable of producing images with sufficient quality. The LB method demonstrates superior image reconstruction accuracy compared to the BB method for all five anatomical sites. With regard to image quality, the MSE metric indiates that the LB method fares better than the BB method while the opposite trend is the case when the PSNR metric is used to evaluate the methods, for all five anatomical sites.

4. Discussion

One advantage of the sparse view CT reconstruction is the low dose delivered to patients. Significant imaging dose reduction can be achieved for patients who undergo multiple CT scans in diagnostic procedures and CBCT scans from image-guided radiation therapy. The proposed method indicates that the imaging dose can potenitally be reduced to $1/7$ of the dose resulting from CT scans using the standard FBP.

The regularization parameter, lambda (λ), determines the relative importance of the data fidelity term in relation to the total variation in the objective function. Lower values putting more weight on TV terms that may result in over-smoothing while higher values putting more weight on data fidelity term that may result in stair-case artifacts and noisy images (Equation 4). Experience from other research indicates that lambda is one of the most influential parameters that affect the image quality and it is likely that no standard lambda value exsits for all image reconstruction scenarios [35]. In practice, since the prior knowldege is usually not available as to what

values are suitable for particular applications, a manual adjustment via trial and error is needed in order to determine optimal lambda values for a particular application. This presents limitations to clinical applications since optimal lambda values are likely dependent on various factors including imaging sites, imaging protocols, the number of projections, etc. since manual adjustment is not clinically feasible. Selection of an optimal regularization parameter value that balances the data fidelity term and the total variation presents challenges for clinicians to achieve improved image quality [35]. Efforts have been expended to optimize the lambda. Alternatively, machine learning methods are applied to find optimal regularization and hyper-parameter values [48, 49].

Our method eliminates the use of the regularization parameter. Instead of constructing an objective function that sums TV and data fidelity term with lambda specifying the relative importance between them, we formulate the problem as a series of sub-problems indexed by iteration k which asymptotically approach the original problem. Only one set of hyper-parameters is used for all image reconstruction cases. The results show that this one set of parameters can adequately reconstrcut the images for most common sites. This is considered a boon for practical application as any efforts to adjust the lambda values are difficult to implement in clinical settings.

The reconstruction computation time is considerably longer. It takes approximately 2 hours (Intel® i7-9700 CPU 3.00 GHz) to complete reconstruction for a 2D image. The computational bottle neck resides in solving the linear equations using the GMRES procedure in which the Newton's method is employed as a subroutine. Although seeking fast implementation of the algorithm is not within the scope of this article, it points to one of future directions as to how we can accelerate this methods.

Our results indicate that the algorithm demonstrates robustness against the noise level typically encountered in the clinical applications. The simulated noise levels are typically from photon number between 10^4 and 10^6. We should be cautioned that the noise study is conducted using the simulated data. The actual noise profile may deviate from Poisson statistics. However, the simluated study gives a clue that the algorithms are robust for several common sites.

Some future directions may be worthwhile to pursue. 1) The parallel GMRES solver may be investigated to solve the linear equations via the Newton's method and may be implemented on GPU platforms [54]. 2) While the lambda parameter is not needed in the logarithmic barrier method, a set of hyper-parameters is used to implement the optimization algorithm. The choice of the hyper-parameters can potentially affect the computing speed and the reconstructed image quality. An optimal set of hyper-parameters that can be used for many clinical sites is desirable. It is likely that noise level, number of projections, acquisition modes and other factors play roles in determining the optimal set.

5. Conclusions

In this article, it has been demonstrated that the compressed sensing technique based on the logatirhmic barrier method is capable of recovering satisfactory images from under-sampled projection data for five common sites: brain, head and neck, lung, prostate, and leg. This method obviates the need of the regularization parameter that specifies the relative weight between the data fidelity and total variation terms in the objective function. Insights have been gained as to implementing the proposed method for clinical imaging applications.

Abbreviations

CT	Computed Tomography
LB	Logarithmic Barrier
rRMSR	Relative Root-Mean Square Error
PSNR	Peak Signal-to-Noise Ratio
MSE	Mean Squared Error
fvFBP	Full-view Filtered Backprojection
svFBP	Sparse-view Filtered Backprojection
BB	Barzilai-Borwein
CBCT	Cone-Beam Computed Tomography
IGRT	Image Guided Radiation Therapy
FBP	Filtered Backprojection
TV	Total Variation
GPU	Graphics Processing Unit
GMRES	Generalized Minimal Residual

Author Contributions

Heping Xu is the sole author. The author read and approved the final manuscript.

Funding

This work is not supported by any external funding.

Conflicts of Interest

The author declares no conflicts of interest.

References

[1] Liguori C, Frauenfelder G, Massaroni C, Saccomandi P, Giurazza F, Pitocco F, Marano R, Schena E. Emerging clinical applications of computed tomography. Medical Devices: Evidence and Research 2015; 8: 265–78. https://doi.org/10.2147/MDER.S70630

[2] Schockel L, Jost G, Seidensticker P, Lengsfeld P, Palkowitsch P, Pietsch H. Developments in X-ray contrast media and the potential impact on computed tomography. Invest Radiol. 2020; 55(9): 592–7. https://doi.org/10.1097/RLI.0000000000000696

[3] Gregoire V, Guckenberger M, Haustermans K, Lagendijk JJW, Menard C, Potter R, Slotman BJ, Tanderup K, Thorwarth D, van Herk M, Zips D. Image guidance in radiation therapy for better cure of cancer. Molecular Oncology. 2020; 14(7): 1470–91. https://doi.org/10.1002/1878-0261.12751

[4] Smith-Bindman R, Lipson J, Marcus R, Kim KP, Mahesh M, Gould R, Berrington de Gonzalez A, Miglioretti DL. Radiation dose associated with common computed tomography examinations and the associated lifetime attributable risk of cancer. Arch Intern Med. 2009; 169(22): 2078–86. https://doi.org/10.1001/archinternmed.2009.427

[5] Kak AC, Slaney M. Principles of computerized tomographic imaging. Switzerland: Society for Industrial and Applied Mathematics; 2001. https://doi.org/10.1137/1.9780898719277

[6] Feldkamp LA, Davis LC, Kress JW. Practical cone-beam algorithm. J. Opt. Soc. Am. A. 1984; 1(6): 612–9. https://doi.org/10.1364/JOSAA.1.000612

[7] Kwon H, Cho J, Oh J, Kim D, Cho J, Kim S, Lee S, Lee J. The adaptive statistical iterative reconstruction-V technique for radiation dose reduction in abdominal CT: comparison with the adaptive statistical iterative reconstruction technique. Br J Radiol. 2015; 88: 20150463. https://doi.org/10.1259/bjr.20150463

[8] Ghetti C, Palleri F, Serreli G, Ortenzia O, Ruffini L. Physical characterization of a new CT iterative reconstruction method operating in sinogram space. J Appl Clin Med Phys. 2013; 14(4): 263–71, https://doi.org/10.1120/jacmp.v14i4.4347

[9] Arapakis I, Efstathopoulos E, Tsitsia V, Kordolaimi S, Economopoulos N, Argentos S, Ploussi A, Alexopoulou E. Using "iDose4" iterative reconstruction algorithm in adults' chest-abdomen-pelvis CT examinations: effect on image quality in relation to patient radiation exposure, Br J Radiol. 2014; 87: 20130613. https://doi.org/10.1259/bjr.20130613

[10] Yu L, Liu X, Leng S, Kofler JM, Ramirez-Giraldo JC, Qu M, Christner J, Fletcher JG, McCollough CH. Radiation dose reduction in computed tomography: techniques and future perspective. Imaging Med. 2009; 1(1): 65–84, https://doi.org/10.2217/iim.09.5

[11] Smith EA, Dillman JR, Goodsitt MM, Christodoulou EG, Keshavarzi N, Strouse P. Model-based iterative reconstruction: effect on patient radiation dose and image quality in pediatric body CT. Radiology. 2014; 270(2): 526–34. https://doi.org/10.1148/radiol.13130362

[12] Liu L. Model-based iterative reconstruction: a promising algorithm for today's computed tomography imaging. Journal of Medical Imaging and Radiation Sciences. 2014, 45: 131-6. https://doi.org/10.1016/j.jmir.2014.02.002

[13] Lu H, Li X, Hsiao IT, Liang Z. Analytical noise treatment for low-dose CT projection data by penalized weighted least-square smoothing in the K-L domain. Proceedings of SPIE, Medical Imaging 2002: Physics of Medical Imaging. 2002; 4682: 146-52. https://doi.org/10.1117/12.465552

[14] Wang J, Li T, Lu H, Liang Z. Penalized weighted least-squares approach to sinogram noise reduction and image reconstruction for low-dose X-ray computed tomography. IEEE Trans Med Imaging. 2006; 25(10): 1272–83. https://doi.org/10.1109/42.896783

[15] La Riviere PJ, Bian J, Vargas PA. Penalized-likelihood sonogram restoration for computed tomography. IEEE Trans Med Imaging. 2006; 25: 1022-36. https://doi.org/10.1109/TMI.2006.875429

[16] Zhu L, Wang J, Xing L. Noise suppression in scatter correction for cone-beam CT. Med Phys. 2009; 36(3): 741-52. https://doi.org/10.1118/1.3063001

[17] Candes EJ, Romberg J, Tao T. Stable signal recovery from incomplete and inaccurate measurements. Communications on Pure and Applied Mathematics. 2006; 59(8): 1207-23. https://doi.org/10.1002/cpa.20124

[18] Candes EJ, Romberg J, Tao T. Robust uncertainty principles: exact signal reconstruction from highly incomplete frequency information. IEEE Transactions on Information Theory. 2006; 52(2): 489-509. https://doi.org/10.1109/TIT.2005.862083

[19] Sidky EY, Pan X, Image reconstruction in circular cone-beam computed tomography by constrained, total-variation minimization. Phys. Med. Biol. 2008; (53): 4777-807. https://doi.org/10.1088/0031-9155/53/17/021

[20] Chen GH, Tang J, Leng S. Prior image constrained compressed sensing (PICCS). Proc SPIE Int Soc Opt Eng. 2008; 6856: 685618. https://doi.org/10.1118/1.2836423

[21] Choi K, Fahimian BP, Li T, Suh TS, Xing L. Enhancement of four-dimensional cone-beam computed tomography by compressed sensing with Bregman iteration. J X-ray Sci Technol. 2013; 21(2): 177-92. https://doi.org/10.3233/XST-130371

[22] Lauzier PT, Tang J, Chen GH. Time-resolved cardiac interventional cone-beam CT reconstruction from fully truncated projections using the prior image constrained compressed sensing (PICCS) algorithm. Phys. Med. Biol. 2012; 57: 2461-76. https://doi.org/10.1088/0031-9155/57/9/2461

[23] Ramirez-Giraldo JC, Trzasko J, Leng S, Yu L, Manduca A, McCollough CH. Nonconvex prior image constrained compressed sensing (NCPICCS): Theory and simulations on perfusion CT. Med Phys. 2011; 38(4) 2157–67. https://doi.org/10.1118/1.3560878

[24] Ma J, Zhang H, Gao Y, Huang J, Liang Z, Feng Q, Chen W. Iterative image reconstruction for cerebral perfusion CT using pre-contrast scan induced edge-preserving prior. Phys. Med. Biol. 2012; 57(22); 7519-42. https://doi.org/10.1088/0031-9155/57/22/7519

[25] Hu Z, Zheng H. Improved total variation minimization method for few-view computed tomography image reconstruction. Biomedical Engineering Online. 2014; 13: 70. https://doi.org/10.1186/1475-925X-13-70

[26] Huang J, Zhang Y, Ma J, Zeng D, Bian Z, Niu S, Feng Q, Liang Z, Chen W. Iterative image reconstruction for sparse-view CT using normal-dose image induced total variation prior. PLoS ONE. 2013; 8(11): e79709. https://doi.org/10.1371/journal.pone.0079709

[27] Zhang H, Ouyang L, Huang J, Ma J, Chen W, Wang J. Few-view cone-beam CT reconstruction with deformed prior image. Med Phys. 2014; 41(12): 121905, https://doi.org/10.1118/1.4901265

[28] Donoho DL. Compressed sensing. IEEE Transactions on Information Theory. 2006; 52(4): 1289-306. https://doi.org/10.1109/TIT.2006.871582

[29] Candes EJ, Wakin MB. An introduction to compressive sensing. IEEE Signal Processing Magazine. 2008; 25(2): 21-30. https://doi.org/10.1109/MSP.2007.914731

[30] Kim H, Chen J, Wang A, Chuang C, Held M, Pouliot J. Non-local total-variation (NLTV) minimization combined with reweighted L1-norm for compressed sensing CT reconstruction. Phys. Med. Biol. 2016; 61: 6878-91. https://doi.org/10.1088/0031-9155/61/18/6878

[31] Zhu L, Niu T, Petrongolo M. Iterative CT reconstruction via minimizing adaptively reweighted total variation. Journal of X-Ray Science and Technology. 2014; 22: 227-40. https://doi.org/10.3233/XST-140421

[32] Xu Q, Yang D, Tan J, Sawatzky A, Anastasio MA. Accelerated fast iterative shrinkage thresholding algorithms for sparsity-regularized cone-beam CT image reconstruction. Med. Phys. 2016; 43(4): 1849-72. https://doi.org/10.1118/1.4942812

[33] Choi K, Wang J, Zhu L, Suh TS, Boyd S, Xing L. Compressed sensing based cone-beam computed tomography reconstruction with a first-order method. Med. Phys. 2010; 37(9): 5113-25, https://doi.org/10.1118/1.3481510

[34] Sun T, Sun N, Wang J, Tan S. Iterative CBCT reconstruction using Hessian penalty. Phys. Med. Biol. 2015; 60: 1965-87. https://doi.org/10.1088/0031-9155/60/5/1965

[35] Park JC, Song B, Kim JS, Park SH, Kim HK, Liu Z, Suh TS, Song WY. Fast compressed sensing-based CBCT reconstruction using Barzilai-Borwein formulation for application to on-line IGRT. Med. Phys. 2012; 39(3): 1207-17. https://doi.org/10.1118/1.3679865

[36] Niu T, Zhu L. Accelerated barrier optimization compressed sensing (ABOCS) reconstruction for cone-beam CT: Phantom studies. Med. Phys. 2012; 39970; 4588-98. https://doi.org/10.1118/1.4729837

[37] Niu T, Ye X, Fruhauf Q, Petrongolo M, Zhu L. Accelerated barrier optimization compressed sensing (ABOCS) for CT reconstruction with improved convergence. Phys. Med. Biol. 2014; 59: 1801-14. https://doi.org/10.1088/0031-9155/59/7/1801

[38] Wieczorek M, Frikel J, Vogel J, Eggl E, Kopp F, Noel PB, Pfeiffer F, Demaret L, Lasser T. X-ray computed tomography using curvelet sparse regularization. Med. Phys. 2015; 42(4): 1555-65. https://doi.org/10.1118/1.4914368

[39] Xu Q, Yu H, Mou X, Zhang L, Hsieh J, Wang G. Low-dose X-ray CT reconstruction via dictionary learning. IEEE Trans Med Imaging. 2012; 31(9): 1682-97. https://doi.org/10.1109/TMI.2012.2195669

[40] Bai J, Liu Y, Yang H. Sparse-view CT reconstruction based on a hybrid domain model with multi-level wavelet transform. Sensors. 2022; 22(9): 3228. https://doi.org/10.3390/s22093228

[41] Jia X, Dong B, Lou Y, Jiang S. GPU-based iterative cone-beam CT reconstruction using tight frame regularization. Phys. Med. Biol. 2011; 56(13): 3787-807. https://doi.org/10.1088/0031-9155/56/13/004

[42] Lohvithee M, Sun W, Chretien S, Soleimani M. Ant colony-based hyperparameter optimisation in total variation reconstruction in X-ray computed tomography. Sensors. 2021; 21: 591. https://doi.org/10.3390/s21020591

[43] Adler J, Oktem O. Learned primal-dual reconstruction. IEEE Transactions on Medical Imaging. 2018; 37(6): 1322-32. https://doi.org/10.1109/TMI.2018.2799231

[44] Baguer DO, Leuschner J, Schmidt M. Computed tomography reconstruction using deep image prior and learned reconstruction methods. Inverse Problems. 2020; 36: 094004. https://doi.org/10.1088/1361-6420/aba415

[45] Jin KH, McCann MT, Froustey E, Unser M. Deep convolutional neural network for inverse problems in imaging. IEEE Transactions on Image Processing. 2017; 26(9): 4509-22. https://doi.org/10.1109/TIP.2017.2713099

[46] Xu H, Sun Q, Luo N, Cao G, Xia D. Iterative nonlocal total variation regularization method for image restoration. PLoS ONE. 2013; 8(6): e65865. https://doi.org/10.1371/journal.pone.0065865

[47] Kamilov U. A parallel proximal algorithm for anisotropic total variation minimization. IEEE Transactions on Image Processing. 2017; 26(2): 539-48. https://doi.org/10.1109/TIP.2016.2629449

[48] Xu J, Noo F. Patient-specific hyperparameter learning for optimization-based CT image reconstruction. Phys. Med. Biol. 2021; 66: 19NT01. https://doi.org/10.1088/1361-6560/ac0f9a

[49] Shen C, Gonzalez Y, Chen L, Jiang SB, Jia X. Intelligent parameter tuning in optimization-based iterative CT reconstruction via deep reinforcement learning. IEEE Transactions on Medical Imaging. 2018; 37(6): 1430-9. https://doi.org/10.1109/TMI.2018.2823679

[50] Xu H. SU-E-I-45, Reconstruction of CT images from sparsely sampled data using logarithmic barrier method. Med. Phys. 2014; 41(6).

[51] La Riviere PJ, Billmire DM. Reduction of noise induced streak artifacts in x ray CT through spline based penalized likelihood sinogram smoothing. IEEE Transactions on Medical Imaging. 2005; 24(1): 105-11. https://doi.org/10.1109/TMI.2004.838324

[52] Boyd S, Vandenberghe L. Convex Optimization, Cambridge University Press; 2004. https://doi.org/10.1017/CBO9780511804441

[53] Barzilai J, Borwein JM. Two-point step size gradient methods. IMA Journal of Numerical Analysis. 1998; 8: 141-8. https://doi.org/10.1093/imanum/8.1.141

[54] He K, Tan SXD, Zhao H, Liu XX, Wang H, Shi G. Parallel GMRES solver for fast analysis of large linear dynamic systems on GPU platforms. INTEGRATION, the VLSI journal. 2016; 52: 10-22. https://doi.org/10.1016/j.vlsi.2015.07.005